

Sensitivity of Delay Doppler Map in Spaceborne GNSS-R to Geophysical Variables of the Ocean

Adriano Camps , Fellow, IEEE, and Hyuk Park , Senior Member, IEEE

Abstract—Global Navigation Satellite Systems reflectometry (GNSS-R) is a particular case of a multistatic radar in which the signals transmitted by navigation satellites are the signals of opportunity. These signals can be processed as a radar scatterometer, as a radar altimeter, or as an unfocused synthetic aperture radar. GNSS-R has shown its potential to infer numerous geophysical variables: over land soil moisture, vegetation height, detection of freeze-thaw state, etc., map sea ice extent and type ..., and over the ocean wind speed and direction, significant wave height, altimetric measurements or even more recently NASA has released a marine plastics litter product, and some also claim that sea surface salinity (SSS) can be inferred. In addition, retrieval algorithms neglect some of the variations of the delay Doppler map (DDM) that are linked to the observation geometry, i.e., look angle with respect to the speed vectors of the transmitter and receiver. All these different effects impact the DDM peak value and its shape, and may affect the retrieval of geophysical parameters, and ultimately the data interpretation. In this study, the following factors impacting the DDM peak value are studied: the observation geometry, the sea surface temperature, and SSS, the 10 m height wind speed (U_{10}) and direction (WD), the presence of foam, the sea development state, the presence of swell, currents, rain, and the presence of oil slicks perturbing the sea surface roughness. This illustrates the complexity of the challenges presented when trying to retrieve some of these variables, the required corrections, and their accuracy.

Index Terms—Delay doppler map, geophysical variables, global navigation satellite systems reflectometry (GNSS-R), ocean, sensitivity.

I. INTRODUCTION

GLOBAL Navigation Satellite Systems reflectometry (GNSS-R) can be understood as a multistatic radar using the signals of opportunity transmitted by navigation satellites. The most generic GNSS-R observable is the so-called “delay

Manuscript received 1 August 2022; revised 16 September 2022; accepted 30 September 2022. Date of publication 5 October 2022; date of current version 13 October 2022. This work was supported in part by the Programa Estatal para Impulsar la Investigación Científico-Técnica y su Transferencia, del Plan Estatal de Investigación Científica, Técnica y de Innovación 2021-2023 (Spain) under Grant PID2021-126436OB-C21, in part by the European Social Fund, and in part by the GENESIS: GNSS Environmental and Societal Missions – Subproject UPC under Grant PID2021-126436OB-C21. (Corresponding author: Adriano Camps.)

Adriano Camps is with the Department of Signal Theory and Communications, Universitat Politècnica de Catalunya–BarcelonaTech, and IEEC/CTE-UPC, 08034 Barcelona, Spain and also as a visiting professor at the UAE University, Al Ain 15551, Abu Dhabi, UAE (e-mail: adriano.jose.camps@upc.edu).

Hyuk Park is with the Department of Physics, Universitat Politècnica de Catalunya–BarcelonaTech, and IEEC/CTE-UPC, 08034 Barcelona, Spain (e-mail: park.hyuk@upc.edu).

Digital Object Identifier 10.1109/JSTARS.2022.3211876

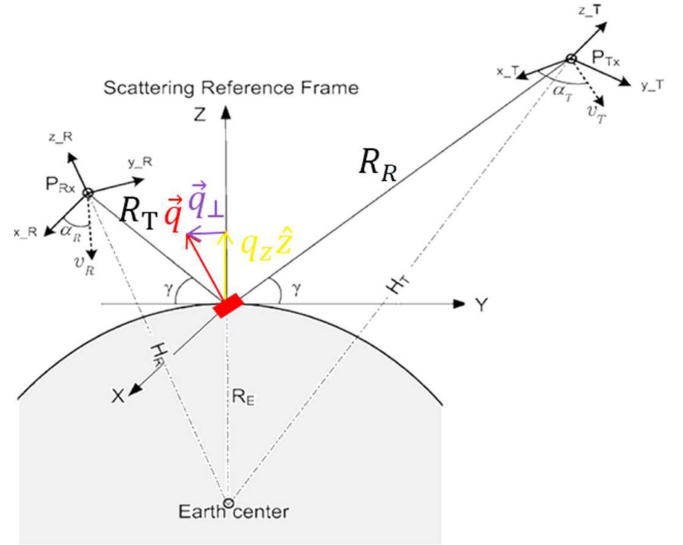


Fig. 1. Scattering reference frame of GNSS-R observation arrangement is used in the simulation. In color, vector \vec{q} is the normal to the tangent plane, and \vec{q}_{\perp} and $q_z \hat{z}$ are the perpendicular and normal components to the surface of the Earth (adapted from [2]).

Doppler map (DDM),” which can be computed as the cross-correlation for different delays (τ) and Doppler frequency shifts (f_d) of the reflected signal, and either a locally generated replica of the transmitted signal in the so-called “conventional” GNSS-R, or with the direct signal itself in the so-called “interferometric” GNSS-R [1]. The cut in the delay domain of the DDM (i.e., constant Doppler frequency) along its peak is called the “waveform (WF).” Fig. 1 shows the scattering geometry of a GNSS-R system.

The DDM can be computed as the sum of two components

$$\left\langle |Y(\tau, f_d)|^2 \right\rangle = \left\langle |Y_c(\tau, f_d)|^2 \right\rangle + \left\langle |Y_i(\tau, f_d)|^2 \right\rangle \quad (1)$$

where $\langle |Y_c(\tau, f_d)|^2 \rangle$ is associated to the coherent scattering component ((5) of [3], or (3), (11), and (12) of [4]), and $\langle |Y_i(\tau, f_d)|^2 \rangle$ to the incoherent scattering component ((3) of [3], or (13) of [4]).

The coherent component is inversely proportional to the square of the total path ($R_T + R_R$ as in Fig. 1), proportional to the power Fresnel reflection coefficient, and proportional to a decorrelation factor equal to $\exp(-4R_a^2)$, being R_a the Rayleigh roughness parameter defined in (12) of [4].

The incoherent component is given by

$$\begin{aligned} \langle |Y_i(\tau, f_d)|^2 \rangle &= \frac{P_T \cdot \lambda^2}{(4\pi)^3} T_c^2 \iint \frac{G_T(\vec{r}) G_R(\vec{r})}{4 \cdot R_T^2(\vec{r}) \cdot R_R^2(\vec{r})} \\ &+ \left| \chi \left(\tau - \frac{R_T(\vec{r}) + R_R(\vec{r})}{c}, f_D(\vec{r}) - f_c \right) \right|^2 \sigma^0(\vec{r}) \cdot d^2 r \end{aligned} \quad (2)$$

where T_c is the coherent integration time; λ is the electromagnetic wavelength, P_T is the transmitted power, G_T and G_R are the transmitter's and receiver's gain in the direction \vec{r} , R_T and R_R are the distances from the transmitter and receiver to the point on the surface \vec{r} , $|\chi(\tau, f)|^2$ is the Woodward ambiguity function, and σ^0 is the normalized bistatic radar cross-section (NBRCS).

Over the open ocean, the DDM is mostly dominated by the incoherent component, and it typically has a “horse shoe” shape, which—in general—is not symmetric, and depends on the relative velocity vectors of the transmitter and receiver (α_T and α_R angles in Fig. 1). If there is first year ice [3] or calm water [5], the coherent component increases, and the DDM has a “K-shape” resulting from the sum of both contributions. Over sea ice and land, the DDM is typically concentrated around the delay and Doppler frequency corresponding to the specular reflection point, and the “tails” are smaller and buried under the noise level due to the lower reflection coefficient. The length of the tails of the DDM, and the trailing edge of the WF are most sensitive to the mean squared slope (mss), which—over the ocean—can be related to the wind speed, and increase for larger mss, as the scattering comes from a larger area (i.e., larger range of delays and Doppler frequencies). The peak of the DDM (or the WF) is sensitive to the mss, but also to the dielectric constant through the scattering coefficient. The variation of the DDM power at the nominal specular point is used to infer, e.g., wind speed over the ocean (e.g., [6]), or soil moisture over land (e.g., [7], [8]).

In many geophysical retrieval algorithms only the dependence NBRCS with the incidence angle is considered. In this study, the dependence of the DDM peak on several parameters is analyzed: the α_T and α_R angles, the wind direction, the presence of swell, and the sea state of development, the sea surface temperature (SST) and salinity, and the presence of oil slicks. To do that the physical optics model for the NBRCS will be computed, which depends on the Fresnel reflection coefficient (\Re), on the probability density function $P()$ (PDF) of the large-scale ($>3\lambda$), and it is given by

$$\sigma^0 = \pi |\Re|^2 \left(\frac{q}{q_z} \right)^4 P \left(\frac{-q_\perp}{q_z} \right) \quad (3)$$

where $-q_\perp/q_z$ is the bidirectional slope of plane normal to \vec{q} (see Fig. 1). The mss of $P()$ is computed from the integral of the sea surface height spectrum ($S(k_x, k_y)$ surface's spectrum) truncated at $k_c = 2\pi/(3\lambda)$

$$\text{mss} = \int k^2 S(k_x, k_y) dk. \quad (4)$$

To the best of our knowledge, there is not a model that parameterizes all these effects in a single sea surface spectrum formulation. For this reason, in this study a Gaussian PDF is

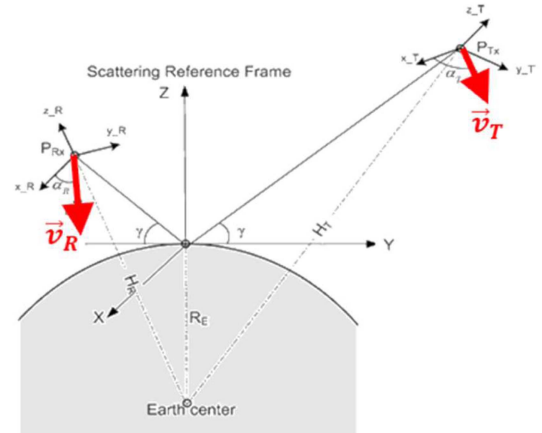


Fig. 2. Definition of the receiver and transmitter speed vectors in the scattering reference frame of GNSS-R observation [15], [16]. In red color, the speed velocity vectors of the receiver and transmitter.

used in (3) with up- and down-wind mss as computed using the Elfouhaily's sea surface height spectrum [9], to account for the effect of wind, wind direction, and fetch, the Durden–Vesecky swell model [10], the Craeye et al. [11] spectrum to account for the effect of the splashes of rain drops, the Huang et al. [12] spectrum to account for the effect of water currents, or the Cox and Munk [13] Gram–Charlier sea surface slopes PDF with Katzberg et al. [14] modifications to assess the impact of the presence of oil slicks. Since this analysis deals with small changes of the DDM peak value due to these perturbations, model limitations and differences are expected to have a minor impact.

II. MATERIALS AND METHODS

In order to do that, the general formulation that relates the instrument, observation geometry, and scene parameters defined in [15], [16] are used.

In all the following simulations, unless otherwise stated, the following parameters have been used, GPS L1 C/A signal, 1 ms coherent integration time, 1 s incoherent integration time, DDMs computed in 100×50 Hz Doppler frequency bins times 100×0.1 C/A chips in delay, α_T and α_R angles equal to 0° , receiver height equal to 500 km, SST equal to 19°C , SSS equal to 35 psu, $\phi_{U10} = 0^\circ$, receiver's bandwidth equal to 2 MHz, and receivers are noise free.

For all scanned variables, results are normalized to the DDM peak of the first value of the sweep ($U_{10} = 2.5$ m/s in the case of the wind speed), except for the impact of oil spills, in which they are normalized to the clean water case.

III. RESULTS

A. Impact of the Relative Speed Vectors

Fig. 2 presents the geometry of the receiver and transmitter speed vectors in the scattering reference frame of GNSS-R observation.

The impact of the α_T and α_R angles is presented in Fig. 3. The angle α_R is set to 0° , while α_T is varied from 0° to 360° . Simulations are conducted for two nominal wind speeds (5 and

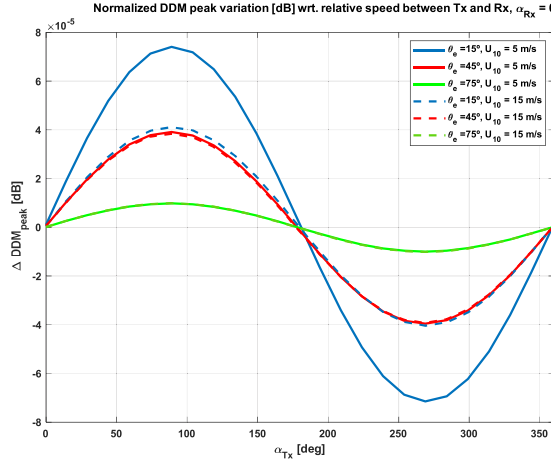


Fig. 3. DDM peak changes due to relative angle between receiver and transmitter speed vectors for 5 and 15 m/s wind speeds, and 15°, 45°, and 75° elevation angles.

15 m/s), and three elevation angles (15°, 45°, and 75°). As it can be appreciated, the variations exhibit a quasinsoidal behavior with α_T , and decrease with increasing wind speed, and increasing elevation angle (θ_e). As it can be appreciated, the largest DDM peak change is $< 10^{-4}$ dB, decreasing in value and sensitivity to wind speed for larger elevation angles. Therefore, this effect is negligible to all the effects.

B. Impact of Wind Speed

Wind is the major disturbing force of the sea surface (see Fig. 4(a), from [17]). However, in order to reach what is called a fully developed sea, wind must be blowing at a constant speed and over a given distance called the fetch. This relationship is shown in Fig. 4(b) from [17]. As the wind speed increases, both the fetch and the wind action time must increase in order to reach those conditions.

Fig. 5(a) shows the total mss computed from the Elfouhaily spectrum [9] (4), and using the Cox and Munk model [13]

$$\text{mss}_{\text{cross-wind}} = 0.003 + 1.92 \cdot 10^{-3} \cdot U_{10} \quad (4a)$$

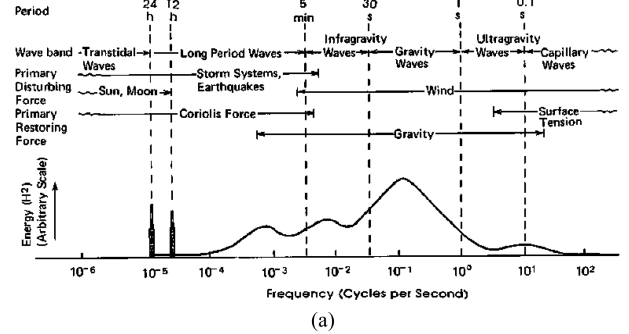
$$\text{mss}_{\text{up-wind}} = 3.16 \cdot 10^{-3} \cdot U_{10}. \quad (4b)$$

Fig. 5(b) shows the computed mss when the wavenumbers are truncated to large-scale ($> 3\lambda$) waves.

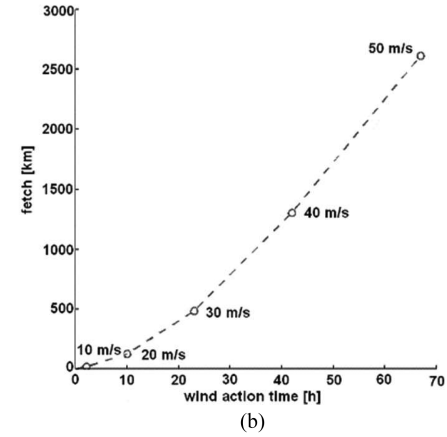
The impact of the wind speed (U_{10}) is presented in Fig. 6. As it is well known, and exploited to infer wind speed, the peak of the DDM rapidly decreases ~ 4.5 dB when the U_{10} increases from 2.5 to ~ 30 m/s. The dependence with the incidence angles is small (≤ 0.3 dB), but not negligible, especially at the largest U_{10} and elevation angles. Note that the model is not including the presence of sea foam, so further (small) reflectivity decreases should be expected if included (see Section II.D).

C. Impact of Wind Direction

The impact of wind direction is examined in Fig. 7(a) and (b) for $U_{10} = 5$ m/s and $U_{10} = 15$ m/s. As it can be seen, in both cases the impact in the DDM peak value is very small, less than ~ 0.01 dB, and therefore can be safely neglected. The wind



(a)



(b)

Fig. 4. (a) Spectral distribution energy of the sea surface roughness. (b) Minimum fetch and duration for a fully developed sea as a function of wind speed (from [17]).

direction is most clearly seen in the asymmetry of tails of the DDM [18].

D. Impact of Sea Foam

In order to estimate the impact of sea foam in the GNSS-R reflectivity, the analytical sea foam emission model presented in [19] is used, which correctly fits the data presented in [20]. The reflectivity change can be estimated as the emissivity change with opposite sign: $\Delta\Gamma = -\Delta e$. At circular polarization, from 25° to 50° incidence angle, the foam emissivity is nearly constant and equal to $e = 0.45$, and emissivity/reflectivity changes are mostly due to the change in sea foam coverage, which is typically very small [21], on the order of 0.3–1% at 15 m/s. Assuming a 1% sea foam coverage, the impact of sea foam is just a ~ 0.02 dB decrease of the reflectivity, and of the peak of the DDM.

E. Impact of Sea State Development

Sea state development is accounted for in Elfouhaily et al. [8] sea surface height spectrum through the inverse-wave-age (Ω_c) parameter. Seas are said to be fully developed, mature, and young when Ω_c has values closed to 0.84, 1, or > 2 , respectively. Fig. 8 shows the computed change in the mss as a function of the wind speed and the inverse-wave-age. As it can be seen, young seas exhibit a much lower mss than fully developed seas, as the long waves have not yet developed. This effect is more noticeable at large wind speeds, as it takes longer time and longer fetches for the sea to develop [see Fig. 4(b)].

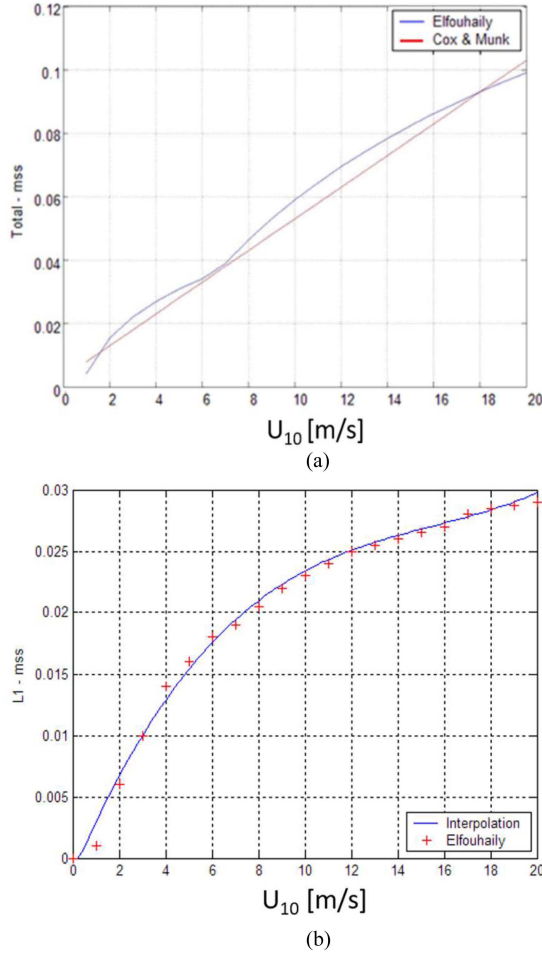


Fig. 5. (a) Total mss and (b) L1 truncated mss computed with Elfouhaily et al. spectrum and Cox and Munk model.

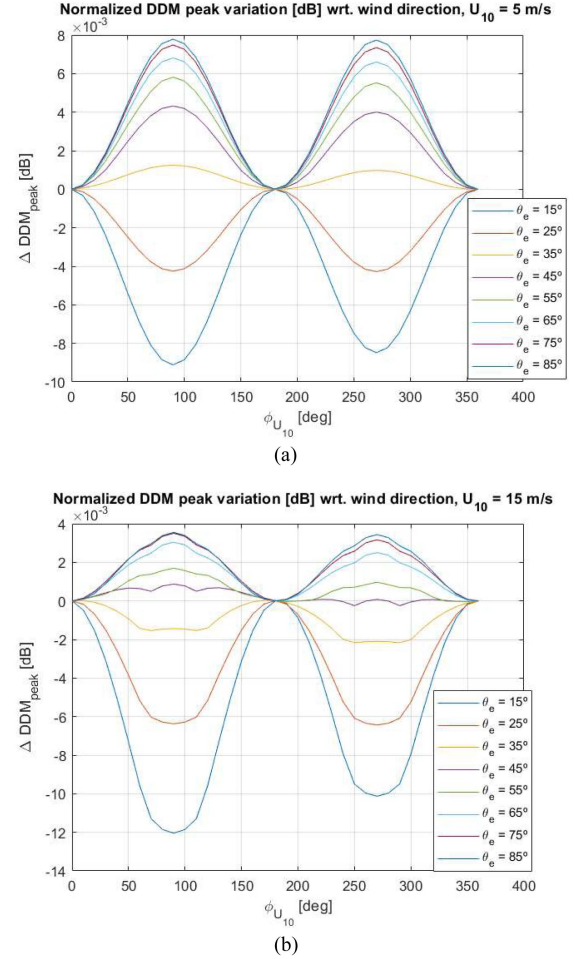


Fig. 7. DDM peak changes due to wind speed (a) and wind direction for $U_{10} = 5 \text{ m/s}$ (b) and $U_{10} = 15 \text{ m/s}$ (b).

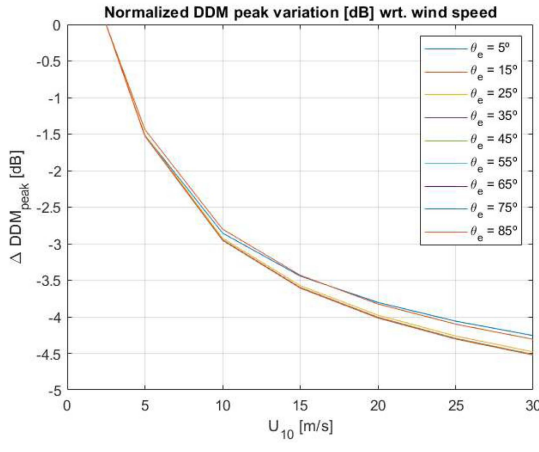


Fig. 6. DDM peak changes due to wind speed.

At $U_{10} = 10 \text{ m/s}$ this mss decrease (sea flattening) ranges from -0.0022 for mature seas to -0.0056 for young-seas, which translates into an increase of the DDM_{peak} from $\sim +0.6$ to $\sim +1.1 \text{ dB}$, respectively. At 20 m/s these effects are much more noticeable because the sea is much less developed; the mss ranges from -0.0088 for mature seas to -0.0225 for young seas,

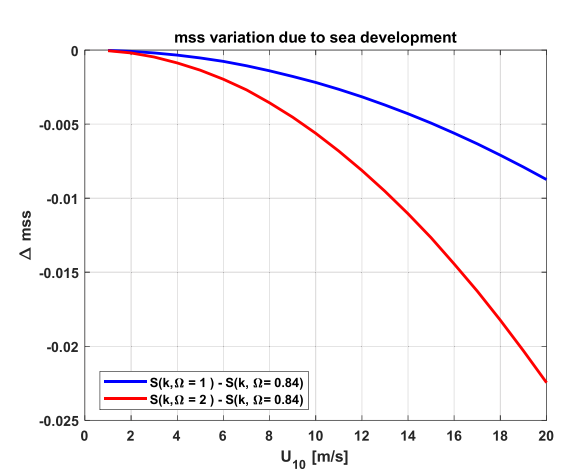


Fig. 8. Variation of the L1 mss due to sea state development. In blue color mature sea ($\Omega_c = 1$) or in red color young sea ($\Omega_c = 2$) minus fully developed seas ($\Omega_c = 0.84$).

which translates into an increase of the DDM_{peak} from $\sim +1.8$ to $\sim +4.1 \text{ dB}$, with small variations (~ 0.1 – 0.2 dB) with the elevation angle.

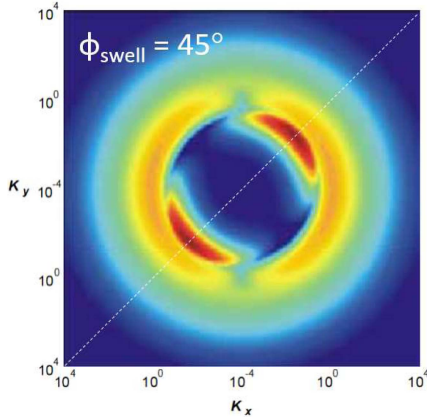


Fig. 9. Sample 2-D sea surface height spectrum including 2-D Gaussian swell for $U_{10} = 7 \text{ m/s}$, $\langle h \rangle = 4 \text{ m}$, $\sigma_x = \sigma_y = 0.0025 \text{ m}^{-1}$, $\lambda_{x,\max} = \lambda_{y,\max} = 300 \text{ m}$, and $\varphi_{\text{swell}} = 45^\circ$ (adapted from [22]).

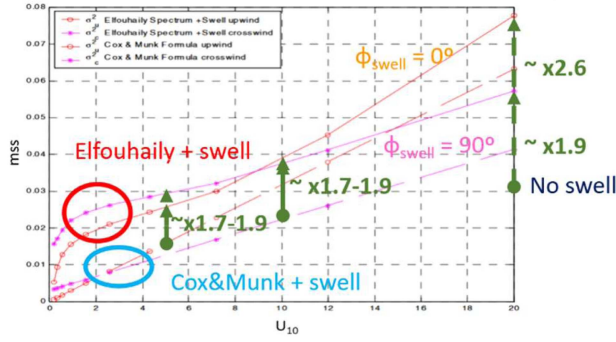


Fig. 10. Swell impact on the mss as a function of the wind speed when swell is in the up-wind or cross-wind directions. Elfouhaily et al. spectrum and 2-D Gaussian swell model used with same parameters, as in Fig. 9.

F. Impact of Swell

Swell refers to the waves that propagate under the predominating influence of gravity, and that have their origin as wind waves originated by distant weather systems, that disperse during the propagation. Swell can modeled as narrowband 2-D Gaussian function as in [10]

$$\Psi_{\text{swell}}(K_x, K_y) = \frac{\langle h^2 \rangle}{2\pi\sigma_x\sigma_y} \cdot \exp \left\{ -\frac{1}{2} \left[\left(\frac{K_x - K_{x,\max}}{\sigma_x} \right)^2 + \left(\frac{K_y - K_{y,\max}}{\sigma_y} \right)^2 \right] \right\} \quad (5a)$$

$$S_{\text{swell}}(K) = K \cdot \int_{-\pi}^{+\pi} \Psi_{\text{swell}}(K, \phi) \cdot d\phi. \quad (5b)$$

Fig. 9 shows a sample 2-D sea surface height spectrum for $U_{10} = 7 \text{ m/s}$, with swell parameters modeled according to [22]: $\langle h \rangle = 4 \text{ m}$, $\sigma_x = \sigma_y = 0.0025 \text{ m}^{-1}$, $\lambda_{x,\max} = \lambda_{y,\max} = 300 \text{ m}$, and $\varphi_{\text{swell}} = 45^\circ$.

Fig. 10 shows the computed mss for the Elfouhaily spectrum including a 2-D Gaussian swell model, as a function of the wind speed, for two swell directions in the up- and cross-wind directions. The mss Cox and Munk model with added swell mss (straight lines) is added for the sake of comparison. The green dots represent the mss values in the absence of swell

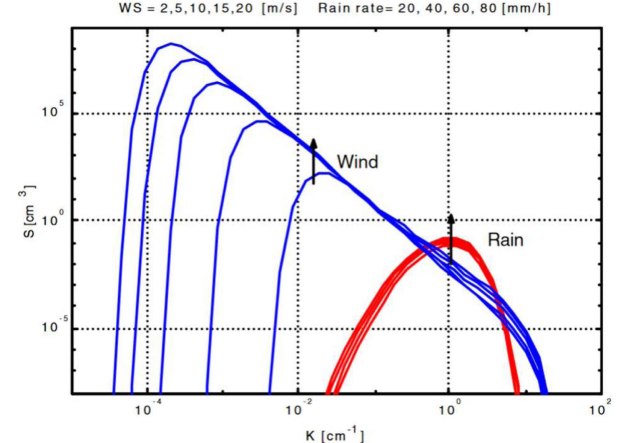


Fig. 11. Elfouhaily et al. wind-induced spectrum for wind speeds 5, 10, 15, and 20 m/s and rain-induced spectrum for rain rates 20, 40, 60, and 80 mm/h (adapted from [24]).

[see Fig. 5(b)] for wind speed 5, 10, and 20 m/s. As it can be appreciated, the mss nearly doubles, for moderate wind speeds up to 5–10 m/s, and more than doubles when the swell is aligned with the wind direction ($\times 2.6$), leading to a decrease in the DDM_{peak} about $\sim -2.3 \dots -2.8 \text{ dB}$ for low to moderate winds, and up to $\sim -2.8 \dots -4.1 \text{ dB}$ at 20 m/s.

G. Impact of Rain

The impact of rain drops splashing on the water surface can be modeled by a log-Gaussian spectrum [11]

$$S_{\text{Rain}}(K) = \frac{1}{2\pi} \cdot v_g(K) \cdot S_{f, \text{peak}} \cdot \exp \left\{ -\pi \left[\frac{\ln(F(K)/F_p)}{\Delta F/F_p} \right]^2 \right\} \quad (6)$$

where v_g is the group velocity [m/s] for the wave-number K , $g = 9.81 \text{ m/s}^2$, $h = 7.445 \times 10^{-5} \text{ m}^3/\text{s}^2$, and the rest of the variables are defined as

$$S_{f, \text{peak}} = 6 \cdot 10^{-4} \cdot R^{0.53} [\text{cm}^2/\text{Hz}] \quad (7)$$

$$\Omega^2 = (2\pi F)^2 = g \cdot K + h \quad (8)$$

$$F_p = 5.772 - 0.0018 \quad (9)$$

and

$$\Delta F = 4.42 + 0.028. \quad (10)$$

In the presence of rain, the wind-induced spectrum combines with the rain-induced spectrum [11], as described in [23]. Fig. 11 shows both spectra for different wind speeds and rain rates. As it can be appreciated, the presence of rain increases mostly the higher frequencies of the spectrum around $K = 1 \text{ cm}^{-1}$.

After both spectra are nonlinearly combined in an iterative way [23], the increase of the mss can be numerically computed using (4). Results are shown in Fig. 12.

For the mss increments shown in Fig. 12, at 3 m/s the increase of the DDM_{peak} is estimated to be $\sim -5.2 \text{ dB}$ at 60 mm/h, and $\sim -2.4 \text{ dB}$ at 20 mm/h. At 10 m/s wind speed, the increase of the DDM_{peak} is $\sim -0.7 \text{ dB}$ at 60 mm/h, and $\sim -0.1 \text{ dB}$ at 20 mm/h,

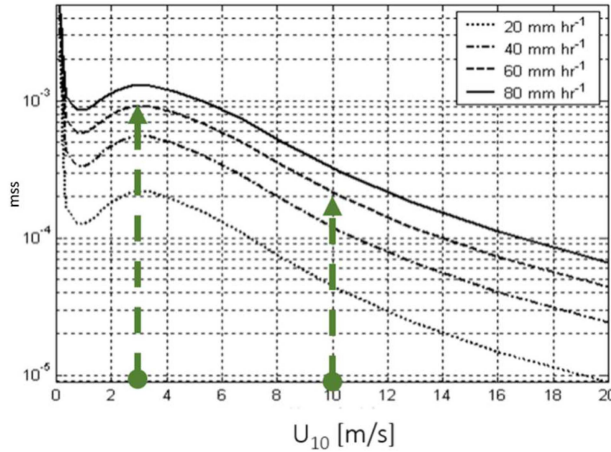


Fig. 12. Rain impact on the mss as a function of the wind speed. The mss increase is computed with respect to rain free conditions for rain rates 20, 40, 60, and 80 mm/h.

and as the wind speed increases, the mss increments are marginal with respect to the mss in rain-free conditions, and therefore the change in the DDM_{peak} is negligible. These large variations of the DDM_{peak} are in agreement with the experimental results presented in [25] and [26].

H. Impact of Surface Currents

The impact of surface currents can be analyzed using the closed-form expression of the Kitaigorodskii–Pierson sea surface height omnidirectional spectrum including the effect of sea surface currents [27]

$$S(K) = \frac{a}{K^3} \cdot \frac{1}{\left(1 + \frac{U_{current}}{c}\right)^7} \cdot \exp \left\{ -\frac{0.74 \cdot g^2}{K^2 \cdot U_{10}^4 \cdot \left(1 + \frac{U_{current}}{c}\right)^4} \right\} \quad (11)$$

where K is the wavenumber, $a = 4.05 \times 10^{-3}$, c is the phase speed, U_{10} is the 10 m height wind speed, and $U_{current}$ is the speed of the current. Fig. 13 shows an example for moderate wind speeds $U_{10} = 5$ m/s, without current, and with a 3 m/s current in favor or against the wind.¹

When the sense of the current is against that of the wind, the spectrum becomes rougher, especially in the long wavenumber (i.e., short waves), and when both current and wind are in the same direction and sense, the spectrum becomes flatter, i.e., the roughness decreases. Computing the mss according to (4), for a much more realistic current of $U_{current} = \pm 0.5$ m/s, the DDM_{peak} changes by $\sim +0.8$ dB/ -1.5 dB at $U_{10} = 1$ m/s, by $\sim \pm 0.3$ dB at $U_{10} = 5$ m/s, and it is negligible beyond $U_{10} = 10$ m/s. Positive sign corresponds to a current in favor of the wind as sea surface becomes flatter, and reflectivity increases, and negative sign correspond to a current against the wind, as sea surface becomes rougher, and reflectivity decreases. This effect is not negligible in calm seas, but it can be safely neglected for wind speed larger than ~ 10 m/s.

¹Maximum ocean surface currents are ~ 1.5 m/s in some areas, such as the Gulf and Kuroshio currents ([https://podaac.jpl.nasa.gov/animations/Ocean-Surface-Current-Speed-from-OSCAR-V2.0]).

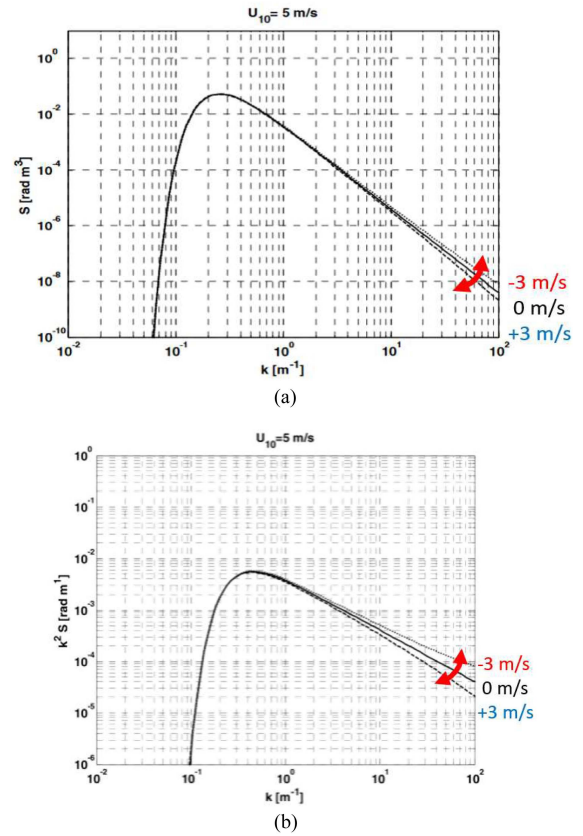


Fig. 13. Sea surface height (left) and slopes (right) spectra at $U_{10} = 5$ m/s for $U_{current} = 3$ m/s (dashed line, red), 0 m/s (solid line, black), and -3 m/s (dotted line, red) (adapted from [28]).

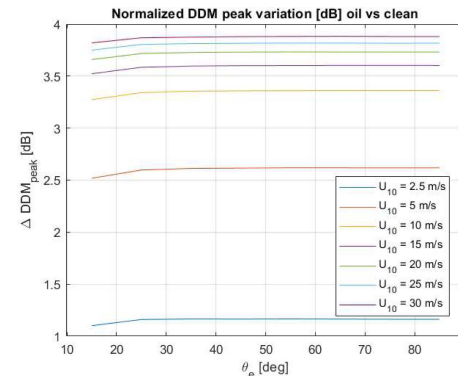


Fig. 14. DDM peak changes due oil spills for different elevation angles, and wind speeds.

G. Impact of Oil Slicks

The impact of oil slicks can be analyzed using the sea surface PDF and mss slopes derived by Cox and Munk [13], which for oil slicks are

$$mss_{cross-wind} = 0.003 + 0.84 \times 10^{-3} \times U_{10} \quad (12a)$$

$$mss_{up-wind} = 0.005 + 0.78 \times 10^{-3} \times U_{10}. \quad (12b)$$

The impact of the presence of oil spills is presented in Fig. 14. The lines represent the increase in the DDM peak due to the

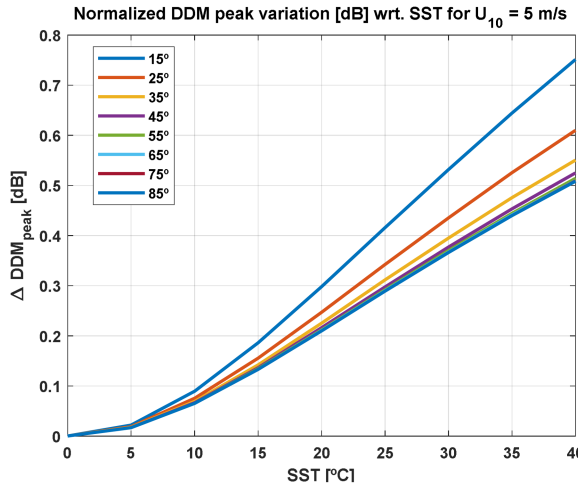


Fig. 15. DDM peak changes due SST for different elevation angles, at $U_{10} = 5$ m/s.

presence of oil, with respect to the DDM computed for the same U_{10} , SSS and SST in clean water. It is worth noting the very significant increase of the DDM peak due to the damping of the capillary waves, which produces a stronger forward scattering. When comparing these results to Fig. 6, for example at $U_{10} = 15$ m/s, the effect of the wind was a decrease of ~ 3.5 dB with respect to $U_{10} = 2.5$ m/s, while now, due to the presence of the oil spill, increases it by ~ 2.5 dB (i.e., 2.5 dB = $3.7 - 1.2$ dB), so the net DDM_{peak} decrease is just ~ 1 dB.

This effect is very important because it illustrates that surfactants or biofouling² transported by ocean currents and accumulated in ocean eddies, or even phytoplankton [29] can similarly produce a significant wave damping effect, leading to anomalous DDM_{peak} increases.

I. Impact of SST

The impact of the SST is presented in Fig. 15. At 10°C , the induced error with respect to 0°C ranges from 0.065 to 0.089 dB depending on the elevation angle, at 20°C from 0.210 to 0.298 dB, and at 30°C from 0.366 to 0.532 dB. This error term cannot be neglected, but it can be easily corrected for using the appropriate SST auxiliary data (e.g., [30]), and precomputed look-up tables with the elevation angle and the wind speed as input variables.

J. Impact of Sea Surface Salinity (SSS)

The impact of the SSS is presented in Fig. 16. The largest DDM variation occurs ~ 25 – 30 psu, with a very small peak variation <0.05 dB, and a variability of 0.02 dB depending on the elevation angle. At 35 psu, the average SSS in the oceans, the absolute DDM variation ranges from -0.02 to -0.04 dB, depending on the elevation angle, i.e., the largest DDM peak sensitivity to SSS is then ~ -0.0017 dB/psu.

²Biofouling is an undesirable accumulation of microorganisms, plants, algae, and animals on submerged structures, such as ship hulls, buoys, but also plastic debris, and other marine litter.

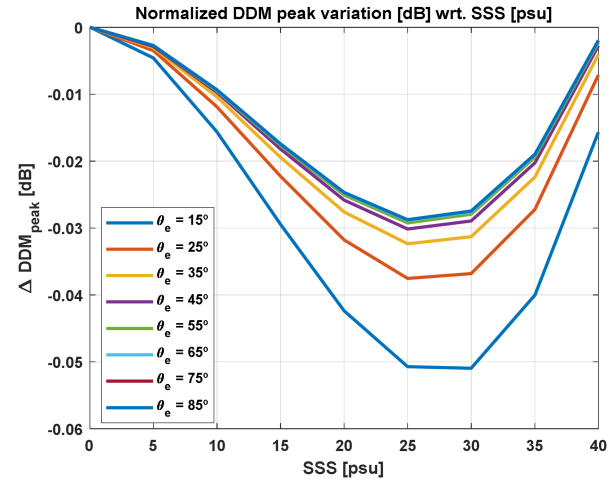


Fig. 16. DDM peak changes due SSS for different elevation angles. No visible differences at $U_{10} = 5$ m/s or 15 m/s.

This effect is indeed very small, but it can be reduced using current SSS maps obtained for example, from ESA SMOS and NASA SMAP missions [31], which offer errors of a fraction of 1 psu. In any case, even without this correction, it has already been proven that the combination of GNSS-R and L-band microwave radiometry data can produce single-pass SSS retrievals with a 0.43 psu error [32].

IV. CONCLUSION

This study has analyzed the sensitivity of the peak of the DDM over the ocean to the relative speed vectors between transmitter and receiver, wind speed and direction, sea foam, SST, and salinity, the perturbations induced by ocean swell, surface currents, rain, or the presence of oil slicks.

Relative angle between transmitter and receiver speed vectors, wind direction, sea foam, and SSS effects are negligible. SST produces changes in the DDM_{peak} up to 0.5–0.75 dB for $SSS = 0 \dots 40$ psu and for all elevation angles, but these changes can be easily corrected for using auxiliary data. The effect of surface currents depends on the background roughness (i.e., wind speed). For example, the DDM_{peak} changes by $\sim +0.8$ dB/ -1.5 dB at $U_{10} = 1$ m/s, and $\sim \pm 0.3$ dB at $U_{10} = 5$ m/s, being negligible above 10 m/s.

The largest impacts are given by the wind speed which decreases the DDM peak by up to 4–4.5 dB at 30 m/s. This effect is exploited to infer wind speed from GNSS-R observations, such as in NASA CYGNSS mission. The second largest is the presence of ocean swell, which may introduce a change in the DDM_{peak} up to 2.3–4.1 dB for $\langle h \rangle = 4$ m, depending on U_{10} . The third largest impact is due to rain rate, notably at low wind speeds, and heavy rains. For example, the DDM_{peak} changes are up to -5.2 dB at $U_{10} = 3$ m/s and $R = 60$ mm/h, decreasing with increasing U_{10} .

Oil spills damp the capillary waves, and increase the forward scattering, compensating to a large extent the decrease induced by the wind-driven roughness. This damping can be also created by surfactants, biofouling, phytoplankton.

NASA recently announced a CYGNSS Ocean Microplastic product [33], [34]. As stated “microplastic concentration number density (#/km²) is estimated by an empirical relationship between ocean surface roughness and wind speed,” but “user caution is advised in regions containing independent, non-correlative factors affecting ocean surface roughness, such as anomalous atmospheric conditions within the Intertropical Convergence Zone, biogenic surfactants (such as algal blooms), oil spills, etc.” Therefore, if the presence of oil spills can be detected by other means (e.g., [35]), its impact in the mss could be estimated, and the DDM peak value corrected, thus improving the estimates of other variables.

REFERENCES

- [1] V. U. Zavorotny, S. Gleason, E. Cardellach, and A. Camps, “Tutorial on remote sensing using GNSS bistatic radar of opportunity,” *IEEE Geosci. Remote Sens. Mag.*, vol. 2, no. 4, pp. 8–45, Dec. 2014, doi: [10.1109/MGRS.2014.2374220](https://doi.org/10.1109/MGRS.2014.2374220).
- [2] H. Park et al., “Retracking considerations in spaceborne GNSS-R altimetry,” *GPS Solut.*, vol. 16, pp. 507–518, 2012, doi: [10.1007/s10291-011-0251-7](https://doi.org/10.1007/s10291-011-0251-7).
- [3] A. Alonso-Arroyo, V. U. Zavorotny, and A. Camps, “Sea ice detection using U.K. TDS-1 GNSS-R data,” *IEEE Trans. Geosci. Remote Sens.*, vol. 55, no. 9, pp. 4989–5001, Sep. 2017, doi: [10.1109/TGRS.2017.2699122](https://doi.org/10.1109/TGRS.2017.2699122).
- [4] V. U. Zavorotny and A. G. Voronovich, “Scattering of GPS signals from the ocean with wind remote sensing application,” *IEEE Trans. Geosci. Remote Sens.*, vol. 38, no. 2, pp. 951–964, Mar. 2000, doi: [10.1109/36.841977](https://doi.org/10.1109/36.841977).
- [5] J. Mashburn, P. Axelrad, C. Zuffada, E. Loria, A. O’Brien, and B. Haines, “Improved GNSS-R ocean surface altimetry with CYGNSS in the seas of Indonesia,” *IEEE Trans. Geosci. Remote Sens.*, vol. 58, no. 9, pp. 6071–6087, Sep. 2020.
- [6] G. Foti et al., “Spaceborne GNSS reflectometry for ocean winds: First results from the U.K. TechDemoSat-1 mission,” *Geophys. Res. Lett.*, vol. 42, pp. 5435–5441, 2015, doi: [10.1002/2015GL064204](https://doi.org/10.1002/2015GL064204).
- [7] A. Camps et al., “Sensitivity of GNSS-R spaceborne observations to soil moisture and vegetation,” *IEEE J. Sel. Topics Appl. Earth Observ. Remote Sens.*, vol. 9, no. 10, pp. 4730–4742, Oct. 2016, doi: [10.1109/JSTARS.2016.2588467](https://doi.org/10.1109/JSTARS.2016.2588467).
- [8] C. Chew, R. Shah, C. Zuffada, G. Hajj, D. Masters, and A. J. Mannucci, “Demonstrating soil moisture remote sensing with observations from the U.K. TechDemoSat-1 satellite mission,” *Geophys. Res. Lett.*, vol. 43, pp. 3317–3324, 2016, doi: [10.1002/2016GL068189](https://doi.org/10.1002/2016GL068189).
- [9] T. Elfouhaily, B. Chapron, K. Katsaros, and D. Vandemark, “A unified directional spectrum for long and short wind-driven waves,” *J. Geophysical Res.*, vol. 102, no. C7, pp. 15 781–15 796, 1997, doi: [10.1029/97JC00467](https://doi.org/10.1029/97JC00467).
- [10] S. Durden and J. Vesecsky, “A physical radar cross-section model for a wind-driven sea with swell,” *IEEE J. Ocean. Eng.*, vol. 10, no. 4, pp. 445–451, Oct. 1985.
- [11] C. Craeye, P. W. Sobieski, and L. F. Bliven, “Scattering by artificial wind and rain roughened water surfaces at oblique incidences,” *Int. J. Remote Sens.*, vol. 18, no. 10, pp. 2241–2246, 1997.
- [12] N. E. Huang, D. T. Chen, C. C. Tung, and J. R. Smith, “Interactions between steady non-uniform currents and gravity waves with applications for current measurements,” *J. Phys. Oceanogr.*, 1972, pp. 420–431.
- [13] C. Cox and W. Munk, “Measurement of the roughness of the sea surface from photographs of the sun’s glitter,” *J. Opt. Soc. Am.*, vol. 44, no. 11, pp. 838–850, Nov. 1954.
- [14] S. J. Katzberg, O. Torres, and G. Ganoe, “Calibration of reflected GPS for tropical storm wind speed retrievals,” *Geophys. Res. Lett.*, vol. 33, 2006, Art. no. L18602, doi: [10.1029/2006GL026825](https://doi.org/10.1029/2006GL026825).
- [15] H. Park et al., “A generic level 1 simulator for spaceborne GNSS-R missions and application to GEROS-ISS ocean reflectometry,” *IEEE J. Sel. Topics Appl. Earth Observ. Remote Sens.*, vol. 10, no. 10, pp. 4645–4659, Oct. 2017, doi: [10.1109/JSTARS.2017.2720625](https://doi.org/10.1109/JSTARS.2017.2720625).
- [16] H. Park, A. Camps, J. Castellvi, and J. Muro, “Generic performance simulator of spaceborne GNSS-Reflectometer for land applications,” *IEEE J. Sel. Topics Appl. Earth Observ. Remote Sens.*, vol. 13, pp. 3179–3191, 2020, doi: [10.1109/JSTARS.2020.3000391](https://doi.org/10.1109/JSTARS.2020.3000391).
- [17] J. A. Knauss, *Introduction to Physical Oceanography*. Hoboken, NJ, USA: Prentice Hall, 1997, Art. no. 309.
- [18] E. Valencia, V. U. Zavorotny, D. M. Akos, and A. Camps, “Using DDM asymmetry metrics for wind direction retrieval from GPS ocean-scattered signals in airborne experiments,” *IEEE Trans. Geosci. Remote Sens.*, vol. 52, no. 7, pp. 3924–3936, Jul. 2014, doi: [10.1109/TGRS.2013.2278151](https://doi.org/10.1109/TGRS.2013.2278151).
- [19] M. D. Anguelova and P. W. Gaiser, “Microwave emissivity of sea foam layers with vertically inhomogeneous dielectric properties,” *Remote Sens. Environ.*, vol. 139, pp. 81–96, 2013, doi: [10.1016/j.rse.2013.07.017](https://doi.org/10.1016/j.rse.2013.07.017).
- [20] A. Camps et al., “The emissivity of foam-covered water surface at L-band: Theoretical modeling and experimental results from the FROG 2003 field experiment,” *IEEE Trans. Geosci. Remote Sens.*, vol. 43, no. 5, pp. 925–937, May 2005.
- [21] E. C. Monahan and M. Lu, “Acoustically relevant bubble assemblages and their dependence on meteorological parameters,” *IEEE J. Ocean. Eng.*, vol. 15, no. 4, pp. 340–349, Oct. 1990, doi: [10.1109/48.103530](https://doi.org/10.1109/48.103530).
- [22] J. Miranda, M. Vall-Ilossera, A. Camps, and N. Duffo, “Sea surface emissivity at L-band: Swell effects,” in *Proc. IEEE Int. Geosci. Remote Sens. Symp.*, 2002, vol. 5, pp. 2623–2625, doi: [10.1109/IGARSS.2002.1026721](https://doi.org/10.1109/IGARSS.2002.1026721).
- [23] C. Craeye, “Radar signature of the sea surface perturbed by rain,” Ph. D. dissertation, Université Catholique de Louvain, Brussels, Belgium, Dec. 1998.
- [24] A. Camps, M. Vall-Ilossera, J. Miranda, and N. Duffo, “Emissivity of the sea surface roughened by rain: Simulation results,” in *Proc. IEEE 2001 Int. Geosci. Remote Sens. Symp.*, 2001, vol. 5, pp. 2433–2435, doi: [10.1109/IGARSS.2001.978026](https://doi.org/10.1109/IGARSS.2001.978026).
- [25] R. Balasubramaniam and C. Ruf, “Characterization of rain impact on L-Band GNSS-R ocean surface measurements,” *Remote Sens. Environ.*, vol. 239, 2020, Art. no. 111607, doi: [10.1016/j.rse.2019.111607](https://doi.org/10.1016/j.rse.2019.111607).
- [26] M. Asgarimehr et al., “Remote sensing of precipitation using reflected GNSS signals: Response analysis of polarimetric observations,” *IEEE Trans. Geosci. Remote Sens.*, vol. 60, 2022, Art. no. 5800412, doi: [10.1109/TGRS.2021.3062492](https://doi.org/10.1109/TGRS.2021.3062492).
- [27] N. E. Huang, D. T. Chen, C. C. Tung, and J. R. Smith, “Interactions between steady non-uniform currents and gravity waves with applications for current measurements,” *J. Phys. Oceanogr.*, vol. 2, pp. 420–431, Oct. 1972, doi: [10.1175/1520-0485\(1972\)002<0420:IBSWUC>2.0.CO;2](https://doi.org/10.1175/1520-0485(1972)002<0420:IBSWUC>2.0.CO;2).
- [28] A. Camps, M. Vall-Ilossera, J. Miranda, and J. Font, “Sea surface brightness temperature at L-band: Impact of surface currents,” in *Proc. IEEE Int. Geosci. Remote Sens. Symp.*, 2004, vol. 5, pp. 3481–3484, doi: [10.1109/IGARSS.2004.1370457](https://doi.org/10.1109/IGARSS.2004.1370457).
- [29] N. Rodriguez-Alvarez and K. Oudrhiri, “The bistatic radar as an effective tool for detecting and monitoring the presence of phytoplankton on the ocean surface,” *Remote Sens.*, vol. 13, 2021, Art. no. 2248, doi: [10.3390/rs13122248](https://doi.org/10.3390/rs13122248).
- [30] NOAA Coast Watch: Sea Surface Salinity. Last Accessed: Jul. 21, 2022. [Online]. Available: <https://coastwatch.noaa.gov/cw/satellite-data-products/sea-surface-temperature.html>
- [31] NOAA Coast Watch: Sea Surface Salinity. Last Accessed: Jul. 21, 2022. [Online]. Available: <https://coastwatch.noaa.gov/cw/satellite-data-products/sea-surface-salinity.html>
- [32] J. F. Munoz-Martin and A. Camps, “Sea surface salinity and wind speed retrievals using GNSS-R and L-Band microwave radiometry data from FMPL-2 onboard the FSSCat mission,” *Remote Sens.*, vol. 13, 2021, Art. no. 3224, doi: [10.3390/rs13163224](https://doi.org/10.3390/rs13163224).
- [33] CYGNSS Ocean Microplastic Concentration (Version 1.0) Release. Last Visited: Jan. 10, 2022. [Online]. Available: <https://podaac.jpl.nasa.gov/announcements/2021-11-24-CYGNSS-Ocean-Microplastic-Concentration-V1.0-Release>
- [34] M. C. Evans and C. S. Ruf, “Toward the detection and imaging of ocean microplastics with a spaceborne radar,” *IEEE Trans. Geosci. Remote Sens.*, vol. 60, 2022, Art. no. 4202709, doi: [10.1109/TGRS.2021.3081691](https://doi.org/10.1109/TGRS.2021.3081691).
- [35] M. Fingas and C. E. Brown, “A review of oil spill remote sensing,” *Sensors*, vol. 18, 2018, Art. no. 91, doi: [10.3390/s18010091](https://doi.org/10.3390/s18010091).